

Equilibrium Temperatures and Directional Emissivity of Sunlit Airless Surfaces With Applications to the Moon

L. Rubanenko¹ , N. Schorghofer² , B. T. Greenhagen³, and D. A. Paige¹¹Department of Earth, Planetary and Space Sciences, University of California, Los Angeles, CA, USA, ²Planetary Science Institute, Tucson, AZ, USA, ³Applied Physics Laboratory, Johns Hopkins University, Laurel, MD, USA**Key Points:**

- We derive equations to calculate the equilibrium temperature distribution of illuminated rough Gaussian surfaces
- Using our model, we estimate the surface roughness of the Moon at ~1 cm lateral scales
- Our model may be used to measure small-scale surface roughness on airless planetary bodies, such as small moons and asteroids

Correspondence to:L. Rubanenko,
liorr@ucla.edu**Citation:**

Rubanenko, L., Schorghofer, N., Greenhagen, B. T., & Paige, D. A. (2020). Equilibrium temperatures and directional emissivity of sunlit airless surfaces with applications to the Moon. *Journal of Geophysical Research: Planets*, 125, e2020JE006377. <https://doi.org/10.1029/2020JE006377>

Received 7 JAN 2020

Accepted 18 MAY 2020

Abstract Solar irradiance dominates the heat flux incident on airless planetary bodies. In thermal equilibrium, surface roughness affects the temperature distribution by changing the incidence angle local to each slope. In order to simulate temperatures and thermal emissions at different phase angles, existing thermophysical models usually employ computationally expensive techniques such as ray tracing. Here we derive the equilibrium surface temperature distribution of sunlit Gaussian rough surfaces, providing an exact solution for the Sun at the zenith and an approximate solution for the general case. We find that although the slope distribution of realistic airless surfaces is often non-Gaussian, their temperature distribution is well modeled assuming a Gaussian slope distribution. We additionally present closed-form expressions that describe the radiation emitted from rough surfaces at different emission angles and employ them to radiometrically estimate the roughness of the lunar surface using measurements obtained by Lunar Reconnaissance Orbiter (LRO) Diviner. Our model may also be applied to studying the roughness of resolved and unresolved surfaces on other airless planetary bodies.

Plain Language Summary The thermal radiation emitted from the lunar surface is affected by roughness on scales much smaller than the scale of topographic features currently resolved by remote sensing instruments. Here we derive equations to predict the temperature distribution of airless surfaces and the infrared brightness they emit at different observation angles. Using our model, we probe the surface roughness of the Moon on centimeter lateral scales, revealing notable differences between the lunar maria and highlands regions. Our model may also be applied to study the roughness of other unresolved planetary bodies, such as asteroids.

1. Introduction

The energy balance on the surface of airless planetary bodies is dominated by radiation, which, in the absence of significant geothermal and atmospheric heat transport, causes steep temperature gradients over short horizontal distances. During the day, the main source of energy is incoming solar radiation (insolation). For slowly rotating planetary bodies with low near-surface thermal inertia, illuminated slopes quickly reach thermal equilibrium with incoming radiation (Bandfield et al., 2015; Spencer, 1990). As a result, the slope angle directly affects the temperature distribution by changing the incident solar flux vector.

The best studied airless planetary body in the solar system is Earth's Moon. A common way to characterize the lunar surface roughness is through its slope distribution (e.g., Kreslavsky et al., 2013; Rosenberg et al., 2011; Smith, 1967). The degree of roughness at a given lateral scale may be described by the root-mean-square (RMS) slope, and the dependence of the roughness on lateral scale is often expressed by a power law whose exponent is related to the well-known Hurst exponent (Hurst, 1951; Schroeder, 2009). On the Moon, the RMS slope increases at smaller lateral scales (Figure 1a).

The Lunar Reconnaissance Orbiter (LRO) studies the lunar surface roughness employing laser altimetry (Smith et al., 2010), visible imagery (Robinson et al., 2010), infrared (IR) emission (Paige et al., 2010), and radar (Nozette et al., 2010). The effect of subpixel topography on the temperature distribution may be numerically or analytically modeled assuming the surface is composed of idealized topographic features. Buhl et al. (1968) described topographic roughness as a collection of hemispherical bowl-shaped cavities and modeled the daytime temperature of the Moon. Later, Ingersoll et al. (1992), Hayne and Aharonson (2015), and others adopted similar methods to model ice stability on the Moon and the dwarf planet Ceres. Another common

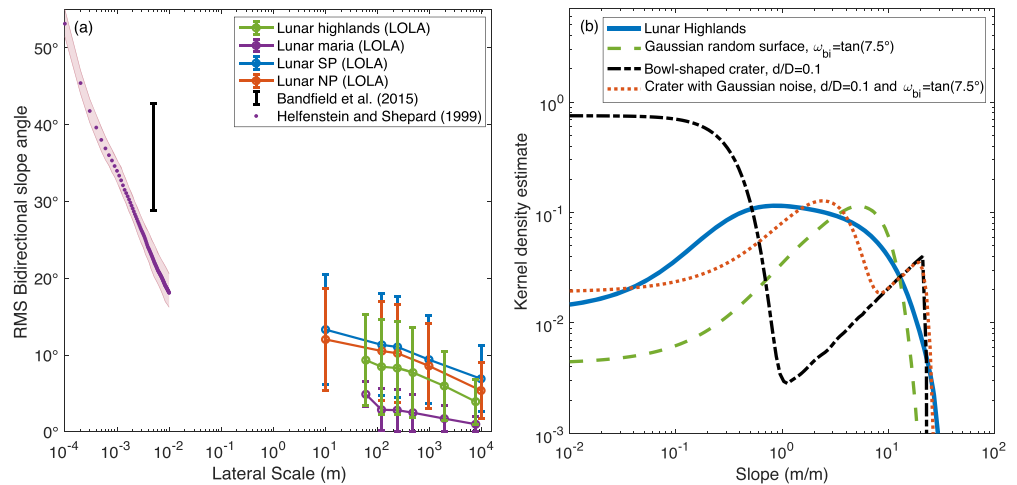


Figure 1. (a) The surface roughness of the Moon decreases with scale. We quantify the surface roughness by calculating the bidirectional RMS slope angle measured using altimetry data obtained by the Lunar Orbiter Laser Altimeter (LOLA). RMS slope on scales <1 cm is based on estimates by Bandfield et al. (2015) and Helfenstein and Shepard (1999). Error bars indicate one standard deviation. SP = south polar region (south of 75°S), NP = north polar region (north of 75°N). (b) The bidirectional (along the slope gradient, see section 2.2) slope angle distribution of the lunar highlands at the 240 m baseline compared to three commonly used artificial surface representations: a Gaussian random surface with the same $\omega_{bi} \approx \tan(7.5^\circ)$, a cratered surface with depth/diameter ratio of 0.1 and a combination of a Gaussian random surface and a cratered surface. The kernel density estimate is an estimate of the probability density function of finite data performed by summing kernel functions, in this case Gaussian (Rosenblatt, 1956).

practice is to assume the surface slopes have a Gaussian distribution (Adler, 2010; Bandfield et al., 2015; Davidsson et al., 2015; Hagfors, 1964; Jamsa et al., 1993; Lagerros, 1997; Li et al., 1999; Rozitis & Green, 2011; Rubanenko & Aharonson, 2017; Smith, 1967). These so-called Gaussian surfaces have uniformly distributed phases in Fourier space and can accommodate any power spectrum and spatial correlation function.

Nearly a century ago, Pettit and Nicholson (1930) and others observed that the emitted thermal radiation flux across the lunar disc decreases more slowly than the cosine of the emission angle expected from a Lambert surface. Similarly, Sinton (1962) measured the infrared brightness of the subsolar point of the Moon and determined its angular dependence is different than that of a Lambert sphere. A few studies have since attempted to explain this deviation. Smith (1967) and Buhl et al. (1968) modeled the effect of surface roughness of unresolved features on the directional emissivity, as different parts of the surface are seen or obstructed when viewed from different observation angles. Others have employed granular scattering (e.g., Hapke, 1981, 1986) or geometric scattering (e.g., Hagfors, 1970; Vogler et al., 1991) to describe this effect, sometimes termed the *thermal phase function*. More recently, Bandfield et al. (2015) compared different spectral channels of the Diviner lunar radiometer experiment on board LRO (Paige et al., 2010) to relate the surface anisothermality to its subpixel RMS slope distribution at the thermal isolation scale. The directional dependence of infrared emissivity has also been studied extensively for terrestrial surfaces (e.g., Sobrino & Cuenca, 1999).

In this work we consider a Gaussian slope distribution and Lambert radiation to model the equilibrium temperature of airless surfaces. In section 2 we derive two separate closed-form models to calculate the equilibrium temperature distribution of sunlit rough Gaussian surfaces and their directional emissivity—the radiation they emit at different emission (observation) angles. In section 3, we apply our models to radiometrically estimate the roughness of the Moon at the thermal isolation scale, which could improve our understanding of its surface composition and how it is affected by various weathering processes.

2. Models and Theory

2.1. Basic Assumptions

In all of the following derivations we assume surface slopes are distributed Gaussian. Even though the slope distribution of realistic surfaces is often non-Gaussian (see Figure 1b and Rosenberg et al., 2011), the temperature distribution of Gaussian surfaces at some scale closely follows that of the realistic lunar topography

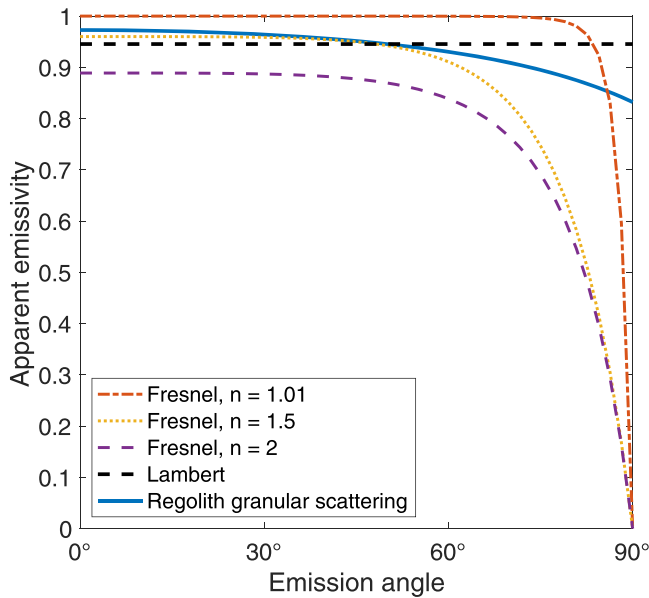


Figure 2. Granular radiative transfer model (blue line) compared to Lambert (black line) and three cases of Fresnel scattering with varying refractive indices. Lambert scattering is an appropriate first-order approximation to granular scattering compared to geometric Fresnel scattering. For the granular scattering model, we assumed a representative asymmetry parameter $g = 0.7$ and single scatter albedo $\tilde{\omega} = 0.5$ (see Appendix A for a detailed explanation). The bolometric emissivity of the Lambert surface was chosen such that it would emit the same average amount of energy as the granular surface.

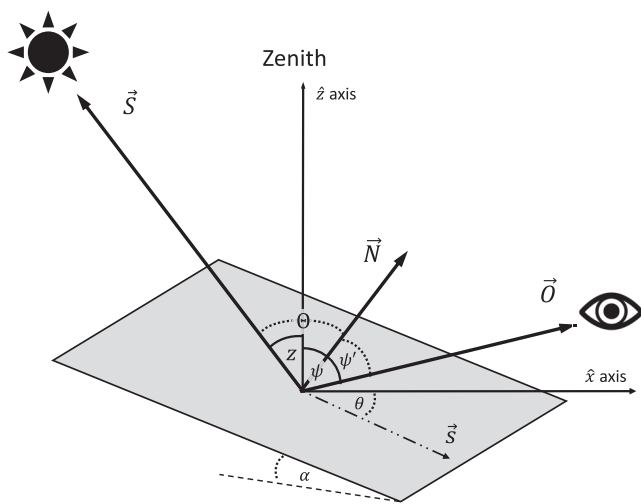


Figure 3. Illustration of vectors and angles used throughout this work. A sloped surface is defined by two angles: the slope angle α and the slope aspect (compass direction) θ . z is the solar zenith angle, and Θ is the angle between the slope normal, \vec{N} and a vector directed at the Sun, \vec{S} . Lower case \vec{s} is the slope vector, defined by the local gradient (see text). ψ is the emission angle and ψ' is the angle between the slope normal vector and a vector directed at the observer, \vec{O} .

at the same scale, making them good statistical analogs for thermal models (e.g., Davidsson et al., 2015; Rubanenko & Aharonson, 2017; Rubanenko et al., 2018). We constrain the impact of this assumption on our results in section 3.1.

To compute thermal emission, we assume a Lambert radiator appropriate for a black body (Howell et al., 2015; Melvin, 1955); that is, that the emitted radiation flux is isotropic and the radiation flux received by an observer depends on the cosine of the angle between the slope normal and the ray connecting the center of the slope to the observer (the local emission angle). From a technical point of view, this assumption greatly simplifies calculations compared to other scattering laws such as Fresnel. From a physical point of view, thermally emitted radiation from the lunar regolith is of the same order as the grain size, and granular scattering approaches geometric-optics limits when the wavelength is much smaller than the size of the particle (Van de Hulst, 1981). Consequently, in many cases assuming Lambertian scattering is as appropriate as Fresnel scattering. To demonstrate this, we compare thermal emission from an optically thick granular material to Fresnel and Lambert scattering.

In Figure 2 we compare the directional emissivity calculated by a simplified particle scattering model with example single scattering albedo and asymmetry parameter (see Appendix A for exact values and discussion) to Lambert and Fresnel phase functions with different refractive indices. We find Lambert is a reasonable first-order approximation for scattering by particulate medium compared to Fresnel given the typical range of incidence angles on a realistic rough surfaces (also see section 2.2.3).

2.2. Equilibrium Temperature Distribution of Gaussian Sunlit Surfaces

A Gaussian stochastic process is a collection of random variables that follow the well-known Gaussian probability density function (PDF):

$$f(x) = \frac{1}{\sqrt{2\pi\sigma^2}} \exp\left[-\frac{(x-\mu)^2}{2\sigma^2}\right], \quad (1)$$

where μ and σ are the mean and standard deviation. A *Gaussian random surface* is a 2-D Gaussian stochastic process, which is both stationary and isotropic in space. For a stationary and isotropic process, the covariance function depends only on the absolute value of the distance between two points and not on their individual locations. The local slope and elevation are not correlated (e.g., Bourlier et al., 2002; Smith, 1967). Consequently, an isotropic Gaussian surface is defined solely by its 1-D covariance function, making it a convenient mathematical analog of realistic topography (Schroeder, 2009).

The height of the topography h of any rough surface may be described in terms of the horizontal Cartesian coordinates x and y . A single slope on the surface is given by the local gradient $\nabla h \equiv \vec{s} = (p, q)$, where $p = \partial h / \partial x$ and $q = \partial h / \partial y$. The slope angle α , the angle between the slope and a flat reference plane, is simply $\tan \alpha = |\vec{s}| = \sqrt{p^2 + q^2}$. The slope aspect, the angle between \vec{s} and the positive direction of the Cartesian x axis (“east”), may be calculated as $\cot \theta = q/p$ (see Figure 3 and Table 1).

For a Gaussian surface, p and q are normally distributed with zero mean and standard deviation ω . For a zero mean process, ω is also the unidirectional slope distribution RMS. It is important to distinguish between

Table 1
Symbols Used in This Work and Their Definitions

Symbol	Definition
α	The slope angle
θ	The slope aspect
p, q	Components of the local elevation gradient \vec{s}
ω	The unidirectional root-mean-square slope
ω_{bi}	The bidirectional root-mean-square slope
Θ	Local incidence angle (between the slope normal and the Sun)
z	Solar zenith angle (between the Sun and the zenith)
a_s	Solar azimuth angle
\vec{N}	The slope normal vector
\vec{S}	A vector between the slope center and the point-Sun
A	The bolometric albedo (0.1)
ϵ	The bolometric emissivity (0.95)
S_0	The solar constant at 1 AU (1,367 W m ⁻²)
B	The infrared brightness
ψ	The global emission angle (between the zenith and the observer)
ψ'	The local emission angle (between the slope normal and the observer)

Note. In parentheses, where applicable, we indicate values assumed throughout this work. Some of these quantities are also illustrated in Figure 3.

the unidirectional RMS slope across a topographic transect, ω , and the bidirectional slope RMS in the direction of the steepest descent, which we abbreviate ω_{bi} . The ratio between those two RMS slope values is $\omega_{bi}/\omega = \sqrt{2}$ (Aharonson & Schorghofer, 2006; Shepard et al., 2001).

The distribution of α is obtained by calculating the joint probability distribution $f_{p,q}$:

$$f_{\alpha}(\alpha) = \frac{\tan \alpha}{\omega^2 \cos^2 \alpha} \exp\left(-\frac{\tan^2 \alpha}{2\omega^2}\right). \quad (2)$$

The distribution of θ for an isotropic surface is simply

$$f_{\theta}(\theta) = \frac{1}{2\pi} \quad (3)$$

we show the full derivation of those distributions in Appendix B1.

In order to find an analytical expression for the equilibrium temperature distribution of rough surfaces, we employ the change of variables technique (see Appendix B2). We first derive expressions relating the slope and aspect angles to the incidence angle and then use them to calculate the surface irradiation and its ensuing equilibrium temperature.

We define the normalized slope normal vector using α and θ as

$$\hat{N} = \frac{\vec{N}}{|\vec{N}|} = (\sin \alpha \cos \theta, \sin \alpha \sin \theta, \cos \alpha) \quad (4)$$

and the solar vector between the slope center and the position of a point-Sun as

$$\hat{S} = (\sin z \cos a, \sin z \sin a, \cos z), \quad (5)$$

where z is the solar zenith angle and a is the solar azimuth angle.

The cosine of the incidence angle Θ , the angle between the slope normal vector and the Sun, is given by the scalar product of Equations 4 and 5:

$$\cos \Theta = \hat{N} \cdot \hat{S} = \cos \alpha \cos z + \sin \alpha \sin z \cos(\theta - a). \quad (6)$$

The solar irradiance, the energy flux received from the Sun, is given by

$$F = \frac{S_0(1-A)}{(r/1 \text{ AU})^2} \cos \Theta \equiv \beta \cos \Theta, \quad (7)$$

where $S_0 = 1,367 \text{ W m}^{-2}$ is the solar constant at 1 AU, A is the bolometric albedo and r is the distance from the Sun. Neglecting scattering and thermal emission, which are small compared to solar radiation (Bandfield et al., 2015), the equilibrium temperature may be derived using the Stefan-Boltzmann law of blackbody radiation:

$$F = \sigma \epsilon T^4, \quad (8)$$

where $\sigma = 5.67 \times 10^{-8} \text{ W m}^{-2} \text{ K}^{-4}$ is the Stefan-Boltzmann constant and ϵ is the bolometric emissivity. Throughout this paper we take $A = 0.1$ and $\epsilon = 0.95$ as example values (Buratti et al., 1996).

2.2.1. Special Case: The Sun at Zenith ($z = 0$)

When the Sun is at zenith, $z = 0$, and Equation 6 may be reduced into $\cos \Theta = \cos \alpha$. In that case, the incidence angle distribution is simply given by Equation 2 with $\alpha = \Theta$. We now use change of variables (see Appendix B2) to obtain the solar irradiance distribution of the surface for $z = 0$:

$$f_{F_0}(F) = f_{\Theta}(\Theta(F)) \frac{\partial \Theta}{\partial F} = \frac{\beta^2}{\omega^2 F^3} \exp\left(-\frac{1}{2\omega^2} \frac{\beta^2 - F^2}{F^2}\right), \quad (9)$$

where F_0 indicates the probability distribution with respect to the incidence flux at $z = 0$. Similarly, the surface equilibrium temperature distribution for $z = 0$:

$$f_{T_0}(T) = f_{F_0}(F(T)) \frac{\partial F}{\partial T} = \frac{4}{\omega^2 \rho^2 T^9} \exp\left(-\frac{1}{2\omega^2} \frac{1 - \rho^2 T^8}{\rho^2 T^8}\right) \quad (10)$$

where T_0 indicates the probability distribution with respect to the equilibrium temperature at $z = 0$ and where we defined $\rho \equiv \sigma \epsilon / \beta$.

A useful result is the mean of the direct irradiance with the Sun at zenith:

$$\bar{F}_0 = \int_0^\beta F f_{F_0}(F) dF = \frac{\beta}{\sqrt{2\omega}} \Gamma\left(\frac{1}{2}, \frac{1}{2\omega^2}\right) \exp\left(\frac{1}{2\omega^2}\right), \quad (11)$$

where $\Gamma(a, x) = \int_x^\infty t^{a-1} e^{-t} dt$ is the upper incomplete gamma function. Note that Γ can be further simplified using the complementary error function, as $\Gamma(1/2, x) = \sqrt{\pi} \text{Erfc}(\sqrt{x})$. Expanding Equation 11 around $\omega = 0$ we find $\bar{F}_0 \approx \beta (1 - \omega^2)$. Since the total absorbed energy is β , this expansion implies a fraction ω^2 is scattered between surface slopes. Similarly, the mean of the temperature distribution is

$$\bar{T}_0 = \int_0^{\rho^{-1/4}} T f_{T_0}(T) dT = \frac{1}{(2\omega^2 \rho^2)^{1/8}} \Gamma\left(\frac{7}{8}, \frac{1}{2\omega^2}\right) \exp\left(\frac{1}{2\omega^2}\right). \quad (12)$$

In section 2.2.3 we compare these derivations with a numerical model and remote sensing data.

2.2.2. The General Case ($z > 0$)

When the Sun is not in zenith, Equation 6 can no longer be reduced as in section 2.2.1. In this case, the incidence angle distribution is,

$$f_{\cos \Theta} = \frac{1}{\pi \omega^2} \exp\left(\frac{1}{2\omega^2}\right) I_{\Theta}(\cos \alpha), \quad (13)$$

where

$$I_{\Theta}(\cos \alpha) = \int_{c_+}^{c_-} \frac{1}{\cos^3 \alpha} \sqrt{\frac{1}{(\cos \alpha - c_+) (c_- - \cos \alpha)}} \exp\left(-\frac{1}{2\omega^2 \cos^2 \alpha}\right) d \cos \alpha, \quad (14)$$

$c_+ = \cos(\Theta + z)$ and $c_- = \cos(\Theta - z)$. Unfortunately, I_{Θ} does not appear to have a closed-form solution. Here we provide an asymptotic approximation using the well-known Laplace method (Bender & Orszag, 2013; Laplace, 1774) that is valid in a variety of cases, later comparing it with the numerical solution

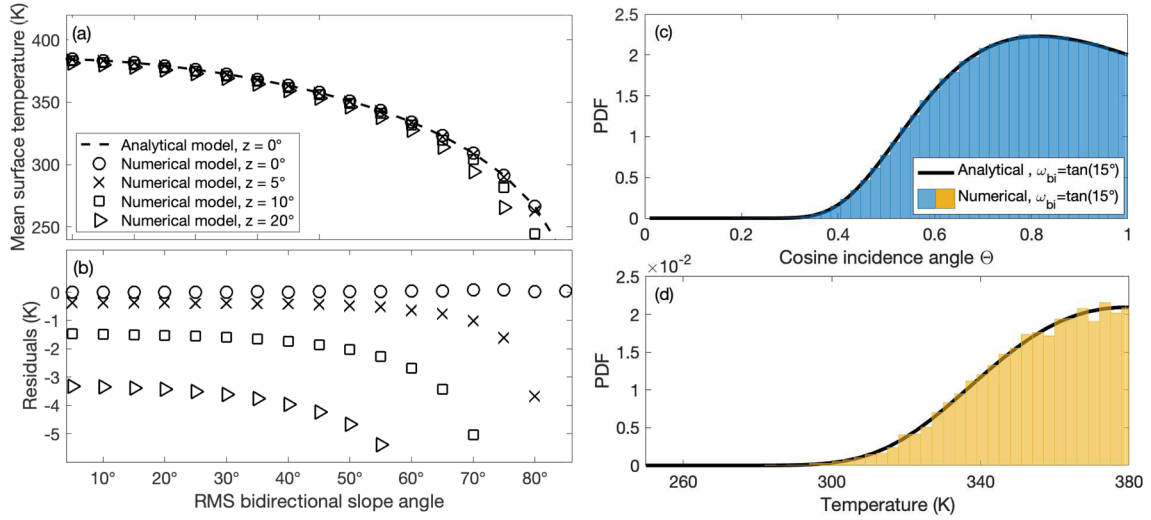


Figure 4. (a) The mean temperature of a Gaussian random surface calculated using our analytical model in the $z = 0$ simplification (dashed line), compared to four different runs of our numerical model with varying zenith angle to show its range of applicability. (b) The residual plot (numeric subtracted from analytic) of panel (a). The prediction made by our analytical model becomes less accurate for higher zenith angles as explained in the text. However, for low to moderate zenith angles and bidirectional RMS slope values, the error is contained at $<1\%$. (c, d) The distributions of the surface incidence angles and equilibrium temperatures calculated by our analytical model (black line) match those calculated by the numerical model (blue and orange bars). For comparison, the temperature of a smooth horizontal surface is 384.80 K.

(see Appendix B3). The asymptotic approximation of $I(v(\Theta))$ is only valid if the product $\omega^2 \cos^2(\Theta - z)$ is sufficiently small. As a result, our solution is more accurate for small ω^2 (low roughness) and $\Theta \approx z$ (Sun-facing surface slopes). We will further explore this parameter space in section 2.2.3.

Using Laplace's method, we approximate the integral and derive an expression for the incidence angle distribution:

$$f_{\cos \Theta}(\Theta) \approx \frac{\omega}{\sqrt{\pi(1 - c_+/c_-)}} \left(1 + \frac{1}{\omega^2 c_-^2}\right) \exp\left[\frac{1}{2\omega^2} \left(1 - \frac{1}{c_-^2}\right)\right]. \quad (15)$$

As before, we use change of variables to derive the irradiance distribution:

$$f_F(F) \approx \frac{\omega}{\sqrt{2\pi\beta^2}} \frac{\sqrt{1 + \Gamma_2 \cot z}}{\Phi_1} \left(1 + \frac{1}{\omega^2 \Phi_3}\right) \exp\left[\frac{1}{2\omega^2} \left(1 - \frac{1}{\Phi_3}\right)\right], \quad (16)$$

and the equilibrium temperature distribution,

$$f_T(T) \approx \frac{4\omega\rho T^3}{\sqrt{2\pi}} \frac{\sqrt{1 + \tau_2 \cot z}}{\tau_1} \left(1 + \frac{1}{\omega^2 \tau_3}\right) \exp\left[\frac{1}{2\omega^2} \left(1 - \frac{1}{\tau_1^2 \tau_3}\right)\right], \quad (17)$$

where Φ_i, τ_i are functions of the irradiance F and temperature T :

$$\begin{aligned} l\Phi_1 &\equiv \sqrt{1 - F^2/\beta^2} & \tau_1 &\equiv \sqrt{1 - \rho^2 T^8} \\ \Phi_2 &= \frac{(F/\beta) \cot z}{\Phi_1} & \tau_2 &= \frac{\rho T^4 \cot z}{\tau_1} \\ \Phi_3 &= \Phi_1^2 (1 + \Phi_2)^2 \sin^2 z & \tau_3 &= \tau_1^2 (1 + \tau_2)^2 \sin^2 z. \end{aligned} \quad (18)$$

Since the integral $\int f_T(T) T dT$ most likely does not have an analytical solution, we do not derive a closed-form expression for the mean equilibrium temperature of Gaussian surfaces in the general case. For the same reason, the above distributions have to be numerically normalized to 1 in order for them to be used as PDFs.

2.2.3. Model Validation and Uncertainties

We validate our analytical model in the $z = 0$ case with a numerical model that accounts for insolation and self shadowing, but not scattering, which may be neglected for low solar incidence angles

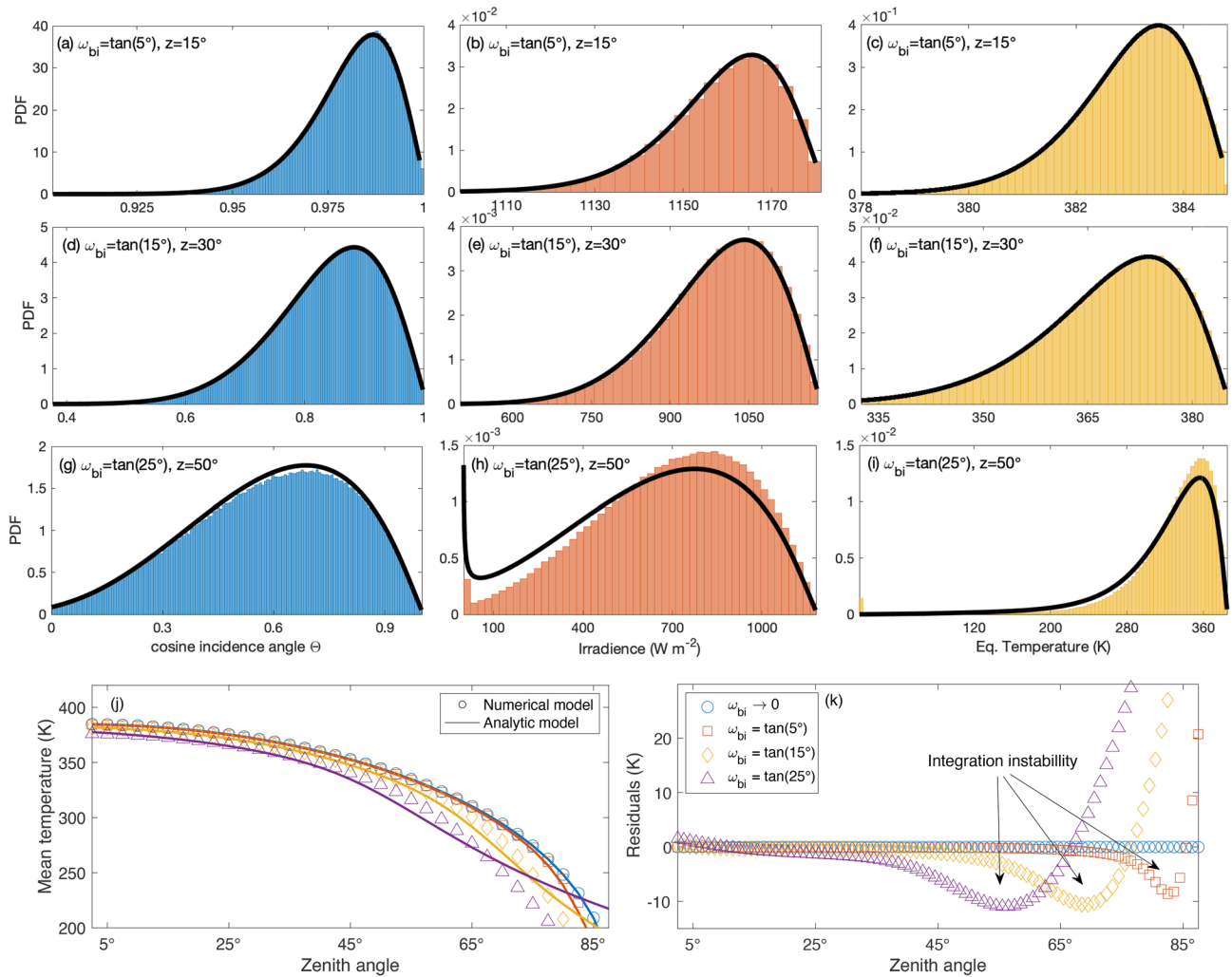


Figure 5. (a–i) Numerically computed incidence angle (blue bars), irradiance (orange bars), and equilibrium temperature (yellow bars) distributions compared with our analytical model (black line) for various values of RMS slope ω_{bi} and zenith angles z . As the surface roughness increases, our approximation of the integral in Equation 14 becomes less accurate. Additionally, as roughness and zenith angles increase, shadows appear on the surface, further skewing our analytical results. (j) The mean surface temperature predicted by our analytical model, compared to a numerical model. (k) Residuals plot for (j), showing the two sources of error in our analytical model.

(Bandfield et al., 2015). In order to numerically calculate the equilibrium temperatures distribution of a Gaussian surface, we generate an artificial Gaussian random field and use Equations 6 through 8 to calculate the incidence angle, irradiance, and temperature for each slope on the field. Self shadows are accounted for by setting the irradiance of all slopes with negative cosine incidence angle to 0. In Figures 4a and 4b we compare the analytically derived to the numerically calculated mean temperature. As expected, our analytic model becomes inaccurate for $z > 0$ as the surface roughness grows and the contribution of the slope aspect to the incidence angle can no longer be neglected (Equations 6). For zero zenith angle the surface is completely illuminated, so shadows do not contribute to the error in Figure 4.

In the general case we no longer assume the solar zenith angle is 0. This generalization carries two major sources of error, one rooted in using Laplace's asymptotic approximation to solve the integral in Equation 14 and the other is related to shadowing.

Laplace's method is more accurate when the coefficient in the exponential function (x in Equation B6) is very large. In our model, this condition holds if both the surface roughness is small and $\Theta \neq z$. Figures 5a–5f show our analytical model agrees well with the numerical model for small roughness and small zenith angles. However, as the surface roughness increases the analytical model becomes less accurate relative to

the numerical model, as demonstrated in Figures 5g–5i. For sufficiently high surface roughness and solar zenith angles, self shadowing affects our predictions as well.

To quantify this error, we compare the mean surface temperature predicted by the analytical and the numerical models in Figures 5j and 5k. The residuals plot shown in Figure 5k demonstrates the two errors discussed above. For a Gaussian surface with $\omega_{bi} = \tan(25^\circ)$, the mean incidence angle roughly equals the solar zenith angle, $z \sim 55^\circ$. For a surface with $\omega_{bi} = \tan(15^\circ)$ this happens at $z \sim 67^\circ$ (see arrows in Figure 5k). At even higher angles, the no-shadows assumption in our analytical model causes it to be warmer compared to the numerical model that includes self-shadowing. Overall, the errors in our approximate analytical model are contained below 10% for $\omega_{bi} < 25^\circ$ and $z < 75^\circ$.

2.3. Thermal Emission From Rough Surfaces Illuminated From Zenith

Due to subresolution topographic roughness, a surface has a distribution of temperatures that is averaged over the footprint of the observing instrument (Shepard, 2017). About a century ago, observers noticed the emitted thermal radiation decreases along the full Moon disk more slowly than the cosine of the emission angle expected from a smooth Lambertian surface (e.g., Pettit & Nicholson, 1930; Saari et al., 1972; Sinton, 1962). This deviation was attributed to topographic relief at the subpixel scale obscuring other thermally emitting surface slopes from the detector.

A few studies have since modeled these effects by numerically integrating the observed brightness, assuming the surface is composed of normally distributed slopes (Smith, 1967) or hemispherical craters (Buhl et al., 1968). In these models, each surface element is assumed to be a perfect Lambertian emitter of infrared radiation, neglecting lateral heat flow and scattering which are less important during the day (Bandfield et al., 2015; Rubanenko & Aharonson, 2017). Other notable studies, such as the comprehensive formalism derived by Hapke (1981), incorporated empirical work with physical scattering laws to provide an approximated closed form description of surface roughness. More recently, Bandfield et al. (2015), Davidsson et al. (2015), Delbo et al. (2015), and others employed computationally expensive numerical models to measure the thermophysical properties of the Moon and other airless planetary bodies. Here we provide a closed-form expression for the average radiation emitted from a rough surface illuminated from zenith as a function of the emission angle.

The infrared brightness of a flat surface is related to the surface temperature as $B = \epsilon\sigma T^4/\pi$ (Buhl et al., 1968). The observed mean brightness $\bar{B}(\psi)$ may be calculated by averaging the total energy reaching the observer from all surface slopes, normalized and divided by the projected area:

$$\bar{B}(\psi) = \frac{\int B \cos \psi' dA}{\int \cos \psi' dA}, \quad (19)$$

where ψ' is the angle between the slope normal vector and the observer (see Figure 3) and the integration is performed only over the part of the surface seen by the observer. As the global emission angle relative to the mean plane ψ increases, a growing number of slopes are obscured from the observer by the topographic relief, reducing $\bar{B}(\psi)$. For an isothermal surface, B is constant regardless of the shape of the surface, and the brightness is constant as expected from a Lambertian surface. This highlights that directional emissivity can be caused by the anisothermality of rough Lambertian surfaces.

For a Gaussian surface illuminated from zenith, we may rewrite Equation 19 as

$$\bar{B}(\psi) = \frac{\bar{B}(0)}{I} \int_{-\infty}^{\infty} \int_{-\infty}^{\infty} \frac{1 - q \tan \psi}{\sqrt{1 + p^2 + q^2}} \exp\left(-\frac{p^2 + q^2}{2\omega^2}\right) S(q, \psi) dpdq, \quad (20)$$

where I is the normalization factor:

$$I = \int_{-\infty}^{\infty} \int_{-\infty}^{\infty} \frac{1}{\sqrt{1 + p^2 + q^2}} \exp\left(-\frac{p^2 + q^2}{2\omega^2}\right) dpdq \quad (21)$$

and $S(q, \psi)$ is the shadowing function after Smith (1967):

$$S(q, \psi) = \frac{H(\cot \psi - q)}{1 + \Lambda(\cot \psi)} \quad (22)$$

where H is the Heaviside step function and

$$\Lambda(\cot \psi) = \frac{1}{2} \left[\sqrt{\frac{2}{\pi}} \frac{\omega}{\cot \psi} \exp\left(-\frac{\cot^2 \psi}{2\omega^2}\right) - \operatorname{erfc}\left(\frac{\cot \psi}{\sqrt{2\omega^2}}\right) \right]. \quad (23)$$

The integral in Equation 20 may be readily reduced to

$$I_B = \int_{-\infty}^{\cot \psi} (1 - q \tan \psi) K_0\left(\frac{1 + q^2}{4\omega^2}\right) \exp\left(\frac{1 - q^2}{4\omega^2}\right) dq, \quad (24)$$

where $K_\nu(x)$ is the ν th-order modified Bessel function of the second kind. To solve this integral, we first separate it into two parts:

$$\begin{aligned} I_{B_1} &= \tan \psi \int_{-\infty}^{\cot \psi} q K_0\left(\frac{1 + q^2}{4\omega^2}\right) \exp\left(\frac{1 - q^2}{4\omega^2}\right) dq \\ &= \frac{\tan \psi + \cot \psi}{2} \exp\left(\frac{1 - \cot^2 \psi}{4\omega^2}\right) \left[K_0\left(\frac{1 + \cot^2 \psi}{4\omega^2}\right) - K_1\left(\frac{1 + \cot^2 \psi}{4\omega^2}\right) \right] \end{aligned} \quad (25)$$

and

$$I_{B_2} = \int_{-\infty}^{\cot \psi} K_0\left(\frac{1 + q^2}{4\omega^2}\right) \exp\left(\frac{1 - q^2}{4\omega^2}\right) dq \quad (26)$$

I_{B_2} most likely has no closed-form solution. However, upon carefully inspecting the derivative of Equation 24 with respect to ψ , we notice that I_{B_1} holds information about the shape of $\bar{B}(\psi)$ while I_{B_2} controls its scale and offset along the vertical axis. As a result, we may obtain an accurate approximate solution to $\bar{B}(\psi)$ by rescaling the solution to the integral I_{B_1} . We first rewrite Equation 20 as

$$\bar{B}(\psi) = \left[\frac{\bar{B}(0) - \bar{B}\left(\frac{\pi}{2}\right)}{\bar{B}(0) - \bar{B}\left(\frac{\pi}{2}\right)} \right] (\bar{B}(\psi) - \bar{B}(0)) + \bar{B}(0) \quad (27)$$

where we defined

$$\tilde{B}(\psi) = \frac{\bar{B}(0)}{2\pi I \omega^2} \frac{I_{B_1}}{1 + \Lambda(\cot \psi)}. \quad (28)$$

and where

$$\tilde{B}(0) = 0 \quad (29)$$

$$\bar{B}\left(\frac{\pi}{2}\right) = \bar{B}\left(\frac{\pi}{2}\right) = \sqrt{\frac{2\pi}{\omega^2}} \frac{\bar{B}(0)}{4\pi I \omega^2} \exp\left(\frac{1}{4\omega^2}\right) \left[K_1\left(\frac{1}{4\omega^2}\right) - K_0\left(\frac{1}{4\omega^2}\right) \right] \quad (30)$$

Overall, we obtain a closed form expression for the thermal radiation emitted by a rough surface illuminated from zenith as a function of the emission angle ψ :

$$\bar{B}(\psi) = \bar{B}(0) - \frac{\bar{B}(0) - \bar{B}\left(\frac{\pi}{2}\right)}{\bar{B}\left(\frac{\pi}{2}\right)} \tilde{B}(\psi) \quad (31)$$

To validate our analytical thermal emission model, we compare it with the numerical solution of the integral in Equation 20 (Figure 6). We find that scaling I_{B_1} provides an excellent approximation to the mean observed brightness $B(\psi)$. We also note that for $\omega \rightarrow 0$, $\bar{B}(\psi)$ becomes constant as expected from a flat (isothermal) Lambert surface.

3. Results: Applications for the Moon

3.1. The Temperature Distribution of Realistic Sunlit Surfaces

A major assumption in our analytical model is that the surface slopes have a Gaussian distribution. However, the slope distribution of the Moon is different from that of a Gaussian rough surface (see Figure 1b above).

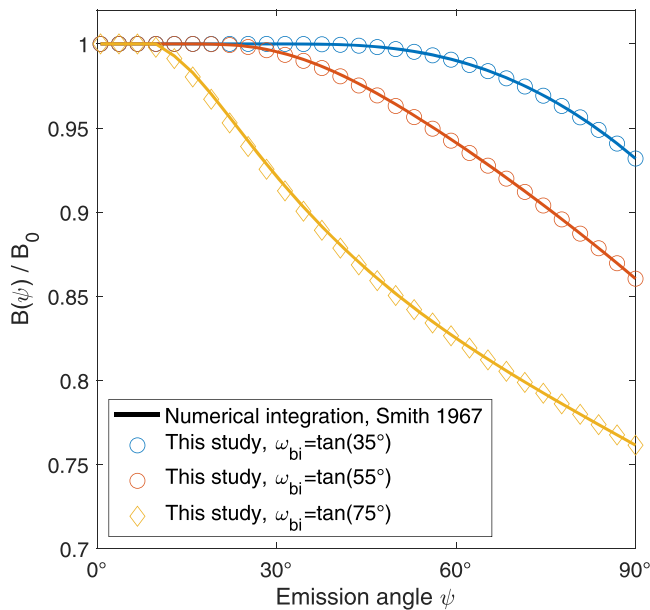


Figure 6. Our closed-form approximation (markers) is in excellent agreement with the complete numerical solution (line) to the integral appearing in Smith (1967) for all values of ω_{bi} .

To assess how this assumption affects the temperature distribution, we again compare our analytical model to a numerical simulation, this time employing realistic topography.

We choose two locations on the Moon whose topographic relief was measured using stereoscopy of Narrow Angle Camera (NAC) image pairs obtained by the Lunar Reconnaissance Orbiter Camera (LROC, Henriksen et al., 2017; Robinson et al., 2010). To avoid thermal effects caused by large-scale slopes, we selected areas that are not dominated by large-scale topographic features. The first region we consider (Figure 7a) is the famous Mandel'shtam scarp, located on the floor of the ~ 200 km Mandel'shtam crater in the highlands region of the Moon (6°N , 162°E). The second site (Figure 7b) is located in the maria region, near the Luna 16 landing site (-0.5°N , 56°E). The bidirectional RMS slope of the highlands site is $\omega_{bi} \approx \tan(9.63^\circ)$ (5 m baseline), and the bidirectional RMS slope of the maria site is, as expected, slightly lower, $\omega_{bi} \approx \tan(4.63^\circ)$ (2 m baseline). The digital terrain models (DTM), constructed using images M191909925 L/R and M191895630 L/R (for Mandel'shtam scarp) and M159582808 L/R and M159589596 L/R (for the Luna 16 landing site), may be downloaded from the planetary data system (PDS).

For each region, we calculate the bidirectional RMS slope ω_{bi} and derive equilibrium temperatures using the numerical model. Then, we feed the calculated ω_{bi} of each surface to our analytical model and derive the temperature distribution for various solar zenith angles. Results are shown in Figure 8. We find that although the slope distributions (Figures 8c and 8e) are significantly different from those of a Gaussian surface, the temperature distributions and their mean predicted by the analytical model are similar to those derived using the numerical model. Consequently, the Gaussian approximation appears to be sufficient when describing the temperatures of realistic rough surfaces.

3.2. Thermal Emission From Rough Surfaces

The lateral scale of the roughness affecting the thermal phase function has been a question of much debate. Smith (1967) suggested the observations conducted by Saari et al. (1966) are mostly affected by large-scale topographic features. By incorporating subsurface conduction in their rough surface model, Spencer (1990), Rozitis and Green (2011), and others noted that the thermal phase function is probably affected by roughness at the thermal isolation scale—which to first order is comparable to the diurnal skin depth. More recently,

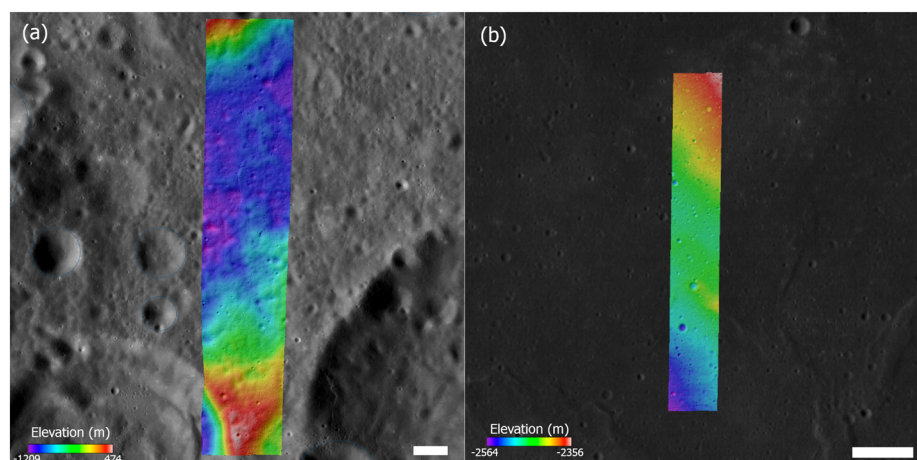


Figure 7. Elevation data for the two lunar sites we considered when comparing the temperature distribution of realistic surfaces relative to Gaussian surfaces (see section 3.1). (a) Highlands region in Mandel'shtam crater (6°N , 162°E). (b) Maria region near the Luna 16 landing site (-0.5°N , 56°E). The colored strips show the stereographically derived DTMs we used and whose resolutions are (a) 5 m/pixel and (b) 2 m/pixel. White scale bar indicates 5 km.

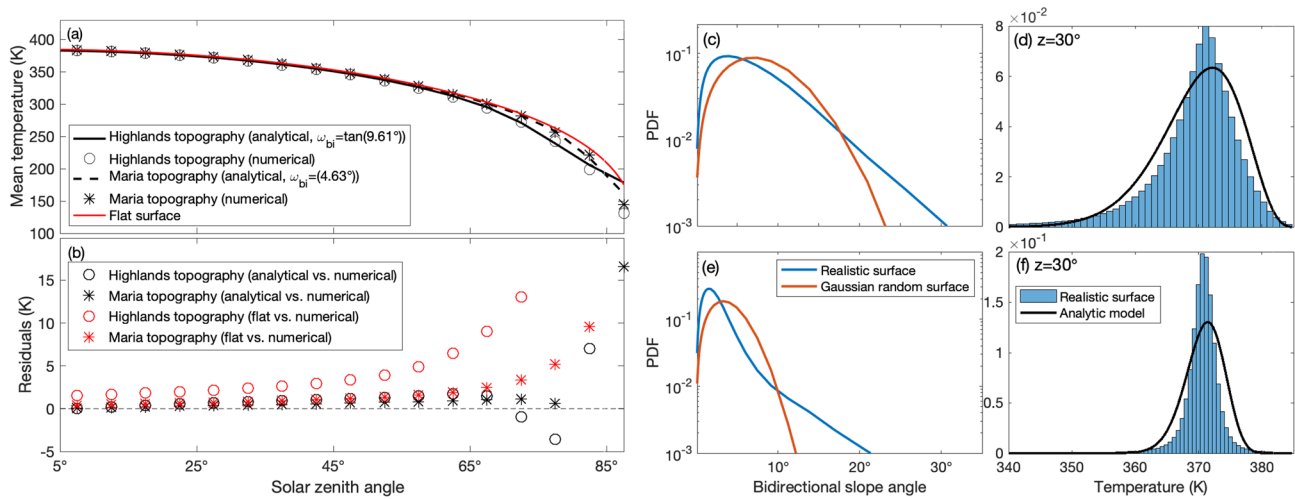


Figure 8. (a) Mean surface temperatures and (b) residuals for the two realistic lunar topographies we consider. Dashed horizontal line indicates zero residuals, for reference. For moderately rough surfaces, our model is more accurate in predicting surface temperatures compared to a model that assumes no roughness at all (red). (c) The slope distribution of the highlands region compared to the slope distribution of a Gaussian random surface. (d) The temperature distribution of the highlands region (blue bars) compared to the temperature distribution of our analytical model (black line). (e, f) Same for maria region.

Bandfield et al. (2015) employed a 2-D thermal conduction model to more accurately constrain the length scale of thermally isolated features on the Moon to $\sim 0.5\text{--}5$ mm.

The RMS slope appearing in our analytical emission model (Equation 31) should thus be treated as the roughness at the scale affecting the thermal phase function. As the scale of this roughness is much smaller than the resolution of thermal observations up to date, it is appropriate to treat it as the thermal equivalent of an optical property of the surface, separate from the roughness of thermally resolved features (as shown, e.g., in Figure 8). To describe this property we introduce the roughness parameter, R , that represents the bidirectional RMS slope at the scale that affects the measured phase function. For detectors with increasing wavelength, R would represent greater lateral scales. Next we use our model to derive R for the lunar surface.

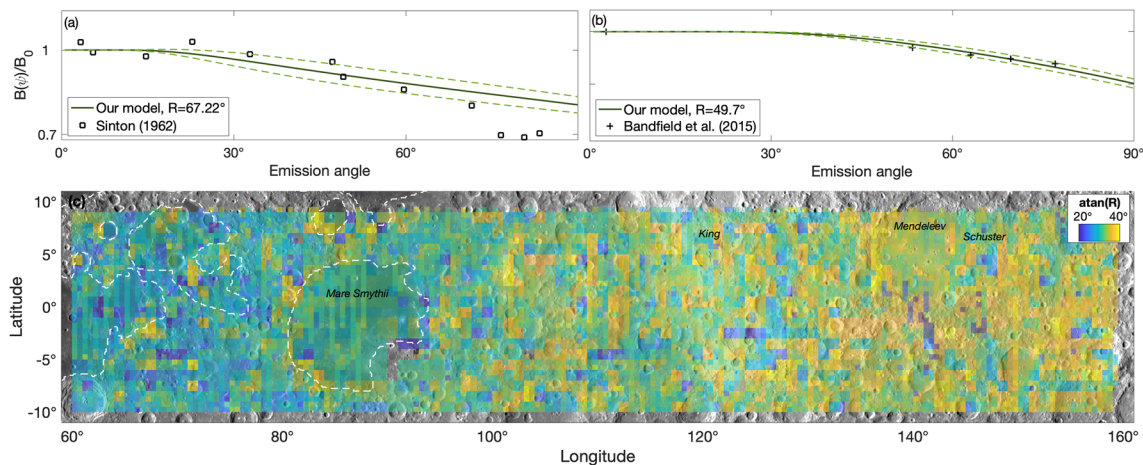


Figure 9. Deriving the surface RMS slope at the thermal isolation scale, which we term R , from infrared brightness data. Unlike large-scale topographic roughness, R more closely resembles an optical property of the surface, affecting its thermal phase function and directional emissivity. (a, b) We use nonlinear regression with Equation 31 as the model function and invert infrared brightness measurements conducted on the Moon by telescope (Sinton, 1962) and LRO Diviner (Bandfield et al., 2015) to find R . Dashed lines indicate 95% confidence intervals. $B(\psi)/B_0$ is the infrared brightness measured at emission angle ψ , normalized by the infrared brightness measured from nadir. (c) The same for Diviner data obtained at different emission angles. As expected, R in the maria region is generally lower than in the highlands region. Notably, the floor of Mare Smythii ($\sim -1^\circ\text{N}$, 85°E) and Mendeleviev Crater ($\sim 5^\circ\text{N}$, 141°E) are smoother than their immediate surroundings. To improve the relatively coarse resolution of the map, which is a consequence of the limited duration of the Diviner off-nadir campaign, we overlaid a $0.5^\circ \times 0.5^\circ$ map (lower transparency) over a $1^\circ \times 1^\circ$ map (higher transparency). The underlying basemap is was generated from LOLA shaded relief data, rebinned at 8 ppd (Speyerer et al., 2011). Dashed lines mark the perimeter of our masked Maria region, which we use to calculate the values in Table 2.

Table 2

Representative Values for R (Bidirectional RMS Slope at the Thermal Isolation Scale) in the Maria, Highlands and the Floors of Mare Smythii and Mendeleev Crater

R	Maria	Highlands	Floor of Mare Smythii	Floor of Mendeleev Crater
Mean	30.2°	36.8°	31.9°	35.0°
Standard deviation	5.9°	4.4°	1.6°	4.3°

Note. Regions were manually masked based on LROC imagery data.

One advantage of our closed-form expression over numerical simulations is that it may be used as a model function for nonlinear fitting. We demonstrate this in Figure 9, where we use nonlinear least squares regression to fit R to two sets of thermal emission measurements. Figure 9a shows telescopic observations of thermal emissions from the lunar surface (Sinton, 1962). Fitting Equation 31 to the data, we obtain $R \approx \tan(67.22^\circ \pm 33.45^\circ)$, where the error indicates 95% confidence intervals. The high relative error is heavily influenced by measurements at high emission angles. For the data in Figure 9b, which shows Diviner observations analyzed by Bandfield et al. (2015), we find $R \approx \tan(49.70^\circ \pm 6.62^\circ)$, in agreement with the RMS slope at the 0.1–10 mm lateral scale measured using DTMs (Helfenstein & Shepard, 1999) and thermally (Bandfield et al., 2015; Rozitis & Green, 2011; Smith, 1967) (Figure 1). The good agreement between our measurements and those obtained using the DTM bolsters the conclusion of Bandfield et al. (2015) who determined Diviner measurements are sensitive to the roughness at the thermal isolation scales.

We apply our results to estimate the Moon's roughness using measurements obtained by Diviner during the off-nadir campaign. We group high emission ($\psi \approx 50^\circ$) and low emission ($\psi < 10^\circ$) channels 3 and 4 brightness temperatures (8.20 ± 0.22 m) in $0.5^\circ \times 0.5^\circ$ and $1^\circ \times 1^\circ$ bins, discarding measurements for which the solar zenith angle was greater than 15° . We elected to use these channels as they closely resemble the bolometric temperatures in the equatorial region of the Moon. Due to the emissivity difference between the Mare and Highlands regions, we used the channel that produced higher average temperatures in low emission angle. Due to the limited duration of the off-nadir campaign, not all the locations in our surveyed area were sampled at the same zenith angle for both high and low emission angles. To suppress that artifact, we correct the measured brightness temperatures by first converting them to energy flux, assuming they are blackbody emitters, and then dividing them by the cosine of the zenith angle in which the measurement was acquired. For each bin, we calculate the thermal phase function and use our model to invert for R . Finally, we remove missing values by interpolating cross-track measurements with a moving median filter with window size of 5 pixels.

In Figure 9 we map R in part of the equatorial region sampled by Diviner during the off-nadir campaign, indicating in Table 2 the mean value for a few selected features. To calculate the average R in the Maria and Highlands regions, we manually mask LROC data, as shown in Figure 9. As expected, R is generally lower in the maria (longitudes ~ 60 – 100°) and higher in the highlands (longitudes ~ 100 – 160°). The good agreement between our measured R and the RMS slope angle measured by Helfenstein and Shepard (1999) at the 0.1–1 mm lateral scale confirms Bandfield et al.'s (2015) conclusions about the lunar thermal isolation scale ($R \sim 30$ – 40°). In the maria, small craters are rougher than their surroundings, potentially due to the presence of small rocks increasing the surface roughness at the thermal isolation lateral scale. The floors of basins such as Mare Smythii ($\sim -1^\circ\text{N}$, 85°E) and Mendeleev Crater ($\sim 5^\circ\text{N}$, 141°E) are slightly smoother than their immediate surroundings but are not distinctly different from similar geologic regions. We note the low resolution of the map in Figure 9 is a consequence of the limited duration of the Diviner off-nadir campaign, and expect to improve it in the future by conducting additional observations.

4. Discussion

Insolation dominates the radiation balance on airless planetary bodies. Surface roughness affects the temperature distribution by scattering incoming radiation and decreasing the downward component of the energy flux vector. Above we derived exact closed-form expressions for the incidence angle, flux, and equilibrium temperature distribution of rough Gaussian surfaces illuminated from zenith (section 2.2.1) and approximate closed-form expressions in the general case (section 2.2.2). Expanding our solution for small ω , we find a fraction $1 - \omega^2$ of the absorbed energy is scattered between surface slopes. Additionally, we find

that although the slope distributions of realistic airless surfaces are often non-Gaussian, their equilibrium temperature distribution closely follows that of a Gaussian surface with the same RMS slope ω .

In addition to changing the temperature distribution, topographic roughness affects the bolometric temperature at emission (observation) angles greater than 0. To account for this effect, we derive a closed-form expression for the directional emissivity of a rough surface illuminated from zenith at any emission angle (section 2.3). Previous studies found that due to the higher roughness at smaller scales, this thermal phase function effect is most likely sensitive to roughness at the thermal isolation scale, which on the Moon is $\sim 0.5\text{--}5$ mm (Bandfield et al., 2015). In order to distinguish the roughness at the thermal isolation scale from roughness of resolved topographic features, we introduce R , the roughness parameter, which corresponds to the bidirectional RMS slope at the thermal isolation scale.

We employ our model to measure R in two cases: telescopic observations and Diviner measurements. While in both cases we find the model agrees well with the observations, a potential deviation occurring at emission angles greater than 70° may imply non-Lambertian scattering on scales smaller than the thermal isolation scale (Bandfield et al., 2015). To measure R for the lunar surface, we fit our model to the thermal phase function measured by Diviner during its off-nadir campaign. We find our estimates for the roughness of the lunar Maria ($R \approx \tan(30.17^\circ)$) and Highlands ($R \approx \tan(36.77^\circ)$) agree well with previous measurements at the 0.1–1 mm lateral scale (Helfenstein & Shepard, 1999). This bolsters Bandfield et al. (2015) findings that Diviner is sensitive to roughness features at this subcentimeter lateral scale. In the future, we intend to increase the resolution of the map we show in Figure 9 by conducting more off-nadir observations using Diviner.

The equations we derived above may be readily applied to estimate the small-scale surface roughness of any airless body whose rotation rate and thermal inertia are sufficiently small. The “thermal parameter” (Spencer, 1990), which combines thermal inertia, rotation rate, and noontime temperature into a single quantity, may be used to test the applicability of our model to other airless surfaces. For example, asteroids whose thermal parameter is close to that of the Moon may be observed from different phase angles (with the Sun in zenith) to estimate their surface roughness at the thermal isolation scale. This in turn may hint at their composition and surface conditions and could help constrain their dynamical parameters.

Appendix A: A Simplified Granular Scattering Model

Scattering by granular media consisting of spherical particles is given by Mie theory. To compute it here, we adapt a 1-D two-stream radiative transfer model originally designed for thermal scattering and emission from optically thick layer of snow grains based on the delta-Eddington approximation (Wiscombe & Warren, 1980). The direct-beam albedo of the grains as a function of the emission angle e is given by

$$a(e) = \frac{\tilde{\omega}^*}{1 + P} \frac{1 - b^* \xi \cos e}{1 + \xi \cos e} \quad (\text{A1})$$

with

$$\begin{aligned} \tilde{\omega}^* &= \frac{(1 - g^2)\tilde{\omega}}{1 - g^2\tilde{\omega}} \\ b^* &= \frac{g^*}{1 - \tilde{\omega}^*g^*} \\ \xi &= \sqrt{3(1 - \tilde{\omega}^*g^*)(1 - \tilde{\omega}^*)} \\ P &= \frac{2\xi}{3(1 - \tilde{\omega}^*g^*)} \\ g^* &= \frac{g}{1 + g} \end{aligned} \quad (\text{A2})$$

where $\tilde{\omega}$ is the single-scatter albedo and $-1 < g < 1$ is the asymmetry parameter of the single-scatter phase function, defined as the mean cosine of the scattering angle. $g = \pm 1$ corresponds to forward-directed or backward-directed scattering and $g = 0$ to isotropic scattering. Here we choose to adopt representative $\tilde{\omega} = 0.5$ and $g = 0.7$, appropriate for Diviner wavelengths and typical lunar regolith grain sizes (Mishchenko, 1994; Wiscombe & Warren, 1980). Finally, albedo is converted to directional emissivity using Kirchhoff's

well-known law of thermal radiation. This result is also stemmed from Helmholtz reciprocity principle that allows to mathematically treat a scattering medium as a thermal emitter.

Geometric scattering is given by the Fresnel equations, which describe directional emissivity by the parallel (s) and the perpendicular (p) components of an electromagnetic wave relative to the plane of incidence. For a perfect dielectric material Fresnel equations only depend on the real part of the refractive index, n ,

$$r_s = \left(\frac{n^2 \cos e - \sqrt{n^2 - \sin^2 e}}{n^2 \cos e + \sqrt{n^2 - \sin^2 e}} \right)^2; r_p = \left(\frac{\cos e - \sqrt{n^2 - \sin^2 e}}{\cos e + \sqrt{n^2 - \sin^2 e}} \right)^2 \quad (\text{A3})$$

we average r_s and r_p to obtain the total Fresnel scattering shown in Figure 2.

Appendix B: Some Derivations

B1. Deriving the Slope and Aspect Distributions

Assuming independence, the joint probability distribution of the normally distributed surface slopes p, q is

$$f(p, q) = \frac{1}{2\pi\omega^2} \exp\left(-\frac{p^2 + q^2}{2\omega^2}\right) dpdq. \quad (\text{B1})$$

For the slope magnitude $s = \sqrt{p^2 + q^2}$ and aspect $\tan \theta = q/p$ the determinant of the Jacobian is trivially s . We use change of variables to find s is Rayleigh distributed with parameter ω ,

$$f(s, \theta) = \frac{s}{\omega^2} \exp\left(-\frac{s^2}{2\omega^2}\right). \quad (\text{B2})$$

Similarly, we use change of variables to find the distribution of the slope angle $\tan \alpha = s$. Since s and θ are independent, it immediately follows that θ is uniformly distributed between 0 and 2π .

B2. The Change of Variable Technique

In order to find the probability distribution of the solar incidence angle given the distributions of the slope angle and slope aspect, we use the well-known change of variables technique (DeGroot & Schervish, 2012).

Let X be a continuous random variable with PDF $f_X(x)$, defined on $[c_1, c_2]$. Let $Y = u(X)$ be an invertible function of X with $X = v(Y)$. The PDF of Y is

$$f_Y(y) = f_X(x) \cdot |v'(y)| \quad (\text{B3})$$

Let X_1, X_2 be two continuous random variables with joint PDF $f_{X_1, X_2}(x_1, x_2)$. Let $Y_1 = u_1(X_1, X_2)$ and $Y_2 = u_2(X_1, X_2)$ be two invertible functions of X_1, X_2 with $X_1 = v_1(Y_1, Y_2)$ and $X_2 = v_2(Y_1, Y_2)$. The joint PDF of Y_1 and Y_2 is

$$f_{Y_1, Y_2}(y_1, y_2) = |J| f(v_1, v_2) \quad (\text{B4})$$

where J is the Jacobian of the transformation and $|J|$ the absolute value of its determinant.

B3. Using Laplace's Method to Find the Asymptotic Approximate of the Incidence Angle Distribution

We obtain an approximate solution to the integral I_Θ appearing in Equation 14 using Laplace's method (Bender & Orszag, 2013). This method, also known as the method of steepest descent, is a technique for obtaining the asymptotic behavior of integrals of the form

$$I(x) = \int_{t_0}^{t_1} f(t) \exp(x\phi(t)) dt. \quad (\text{B5})$$

Laplace's method states that if $\phi(t)$ has a nonzero maximum at $t = m$ on the interval $t_0 \leq t \leq t_1$, then only the immediate neighborhood of this maximum contributes to the asymptotic expansion of $I(x)$ for large x . If these conditions are met, $I(x)$ may be approximated as

$$I(x) \sim \sqrt{\frac{2\pi}{-x\phi''(m)}} f(m) \exp(x\phi(m)) \text{ as } x \rightarrow \infty. \quad (\text{B6})$$

- Robinson, M., Brylow, S., Tschimmel, M., Humm, D., Lawrence, S., Thomas, P., et al. (2010). Lunar reconnaissance orbiter camera ("LROC") instrument overview. *Space Science Reviews*, *150*(1–4), 81–124.
- Rosenblatt, M. (1956). Remarks on some nonparametric estimates of a density function. *The Annals of Mathematical Statistics*, 832–837.
- Rosenburg, M. A., Aharonson, O., Head, J. W., Kreslavsky, M. A., Mazarico, E., Neumann, G. A., et al. (2011). Global surface slopes and roughness of the Moon from the lunar orbiter laser altimeter. *Journal of Geophysical Research*, *116*, E02001. <https://doi.org/10.1029/2010JE003716>
- Rozitis, B., & Green, S. F. (2011). Directional characteristics of thermal–infrared beaming from atmosphereless planetary surfaces—A new thermophysical model. *Monthly Notices of the Royal Astronomical Society*, *415*(3), 2042–2062.
- Rubanenko, L., & Aharonson, O. (2017). Stability of ice on the Moon with rough topography. *Icarus*, *296*, 99–109.
- Rubanenko, L., Mazarico, E., Neumann, G., & Paige, D. (2018). Ice in micro cold traps on Mercury: Implications for age and origin. *Journal of Geophysical Research: Planets*, *123*, 2178–2191. <https://doi.org/10.1029/2018JE005644>
- Saari, J. M., Shorthill, R., & Deaton, T. (1966). Infrared and visible images of the eclipsed Moon of december 19, 1964. *Icarus*, *5*(1-6), 635–659.
- Saari, J. M., Shorthill, R. W., & Winter, D. F. (1972). The sunlit lunar surface. *The Moon*, *5*(1–2), 179–199.
- Schroeder, M. (2009). *Fractals, chaos, power laws: Minutes from an infinite paradise*. New York, NY: Dover Publications.
- Shepard, M. K. (2017). *Introduction to planetary photometry*. Cambridge, UK: Cambridge University Press.
- Shepard, M. K., Campbell, B. A., Bulmer, M. H., Farr, T. G., Gaddis, L. R., & Plaut, J. J. (2001). The roughness of natural terrain: A planetary and remote sensing perspective. *Journal of Geophysical Research*, *106*(E12), 32,777–32,795.
- Sinton, W. M. (1962). Temperatures on the lunar surface. *Physics and astronomy of the Moon* (pp. 407–428). New York, NY: Academic Press New York.
- Smith, B. G. (1967). Lunar surface roughness: Shadowing and thermal emission. *Journal of Geophysical Research*, *72*(16), 4059–4067.
- Smith, D. E., Zuber, M. T., Jackson, G. B., Cavanaugh, J. F., Neumann, G. A., Riris, H., et al. (2010). The lunar orbiter laser altimeter investigation on the lunar reconnaissance orbiter mission. *Space Science Reviews*, *150*(1-4), 209–241.
- Sobrinho, J. A., & Cuenca, J. (1999). Angular variation of thermal infrared emissivity for some natural surfaces from experimental measurements. *Applied Optics*, *38*(18), 3931–3936.
- Spencer, J. R. (1990). A rough-surface thermophysical model for airless planets. *Icarus*, *83*(1), 27–38.
- Speyerer, E., Robinson, M., Denevi, B., & LROC Science Team (2011). Lunar reconnaissance orbiter camera global morphological map of the Moon, *Paper presented at the 42nd Lunar Planetary Science Conference* (Vol. 42, pp. 2387). Houston, TX: Lunar and Planetary Science Conference.
- Van de Hulst, H. C. (1981). *Light scattering by small particles*. New York, NY: Dover Publications.
- Vogler, K. J., Johnson, P. E., & Shorthill, R. W. (1991). Modeling the non-grey-body thermal emission from the full moon. *Icarus*, *92*(1), 80–93.
- Wiscombe, W. J., & Warren, S. G. (1980). A model for the spectral albedo of snow. I: Pure snow. *Journal of the Atmospheric Sciences*, *37*(12), 2712–2733.